Geochemical Journal, Vol. 50, pp. 539 to 555, 2016 doi:10.2343/geochemj.2.0419

Geology and geochemistry of ferromanganese nodules in the Japanese Exclusive Economic Zone around Minamitorishima Island

Shiki Machida,[1,2]* Koichiro Fujinaga,[2,3] Teruaki Ishii,[4] Kentaro Nakamura,[5] Naoto Hirano[6] and Yasuhiro Kato[1,2,3,5]*

[1]Research and Development (R&D) Center for Submarine Resources, Japan Agency for Marine-Earth Science and Technology (JAMSTEC), Natsushima-cho 2-15, Yokosuka, Kanagawa 237-0061, Japan
[2]Frontier Research Center for Energy and Resources, School of Engineering, The University of Tokyo, 7-3-1 Hongo, Bunkyo-ku, Tokyo 113-8656, Japan
[3]Ocean Resources Research Center for Next Generation, Chiba Institute of Technology, 2-17-1 Tsudanuma, Narashino, Chiba 275-0016, Japan
[4]Fukada Geological Institute, 2-13-12 Honkomagome, Bunkyo-ku, Tokyo 113-0021, Japan
[5]Department of Systems Innovation, School of Engineering, The University of Tokyo, 7-3-1 Hongo, Bunkyo-ku, Tokyo 113-8656, Japan
[6]Center for Northeast Asian Studies, Tohoku University, Kawauchi 41, Aoba-ku, Sendai 980-8576, Japan

(*Received February 2, 2015; Accepted February 4, 2016*)

A dense field of ferromanganese (Fe-Mn) nodules was discovered on a seamount approximately 300 km east of Minamitorishima Island, in the Japanese Exclusive Economic Zone. To evaluate its potential as a resource for critical metals, we describe results of a geological survey using the *SHINKAI 6500* submersible (dive No. 6K 1207) during cruise YK10-05 of *R/V Yokosuka* in 2010, and geochemical analyses of collected samples. Submersible observations showed that spherical nodules 5–10 cm in diameter almost fully cover the region of high acoustic reflectivity. The large nodules generally consist of three concentric layers: the outermost mottled (sediment-filled) layer L0, the massive black layer L1, and the innermost porous (sediment-filled) layer L2. Elements including Fe, Ti, Co, As, rare earth elements other than Ce, Th, U, and Pb are concentrated in the nodule rim rather than the center. In contrast, Mn, Al, P, Ca, Ni, Zn, Y, Mo, Ce, and W are concentrated in the center, and decrease toward the rim. Geochemical and structural features indicate that the nodules are compositionally and morphologically similar to Fe-Mn crusts, suggesting that they owe their origin solely to prolonged hydrogenetic precipitation of Fe-Mn-(oxyhydr)oxides. As the nodules include metals of economic interest, especially Co, Ni, Mo, and W, this deposit should have high potential for future mining. The changes in nodule composition from the center to the rim may yield information on paleoceanographic events since early Oligocene time.

Keywords: ferromanganese nodule, critical metals, high acoustic reflectivity, exclusive economic zone, Minamitorishima Island

Introduction

Ferromanganese (Fe-Mn) nodules have long been considered a potential resource for metals, such as Ni, Cu, Co, and Li, that are important in contemporary technology (e.g., Hein *et al*., 2010, 2013). Extensive areas of densely distributed high-grade nodules have been recognized in the region between the Clarion and Clipperton Fracture Zones (CCZ) in the central Pacific Ocean (e.g., Hein *et al*., 2013). Japan has approved exploration licenses for future mining in the CCZ, although the location's remoteness is an obstacle to mining operations. However, large Fe-Mn nodules have also been found to be densely distributed on a seamount in the eastern part of the Japanese Exclusive Economic Zone (EEZ) around Minamitorishima (Marcus) Island, Japan, where their resource potential is more promising because they are located closer to the main islands of Japan than the CCZ. Thus, further exploration in the EEZ can be expected, along with future development followed by the self-sufficiency and the stabilization of the market for critical metals. In this report, we describe results of a geological survey using the submersible *SHINKAI 6500* and a multiple narrow-beam echo sounder system during cruise YK10-05 of *R/V Yokosuka*. We also present the results of chemical analyses to define geochemical features for representative Fe-Mn nodules and adjacent Fe-Mn crusts.

*Corresponding authors (e-mail: m-shikit@jamstec.go.jp; ykato@sys.t.u-tokyo.ac.jp)

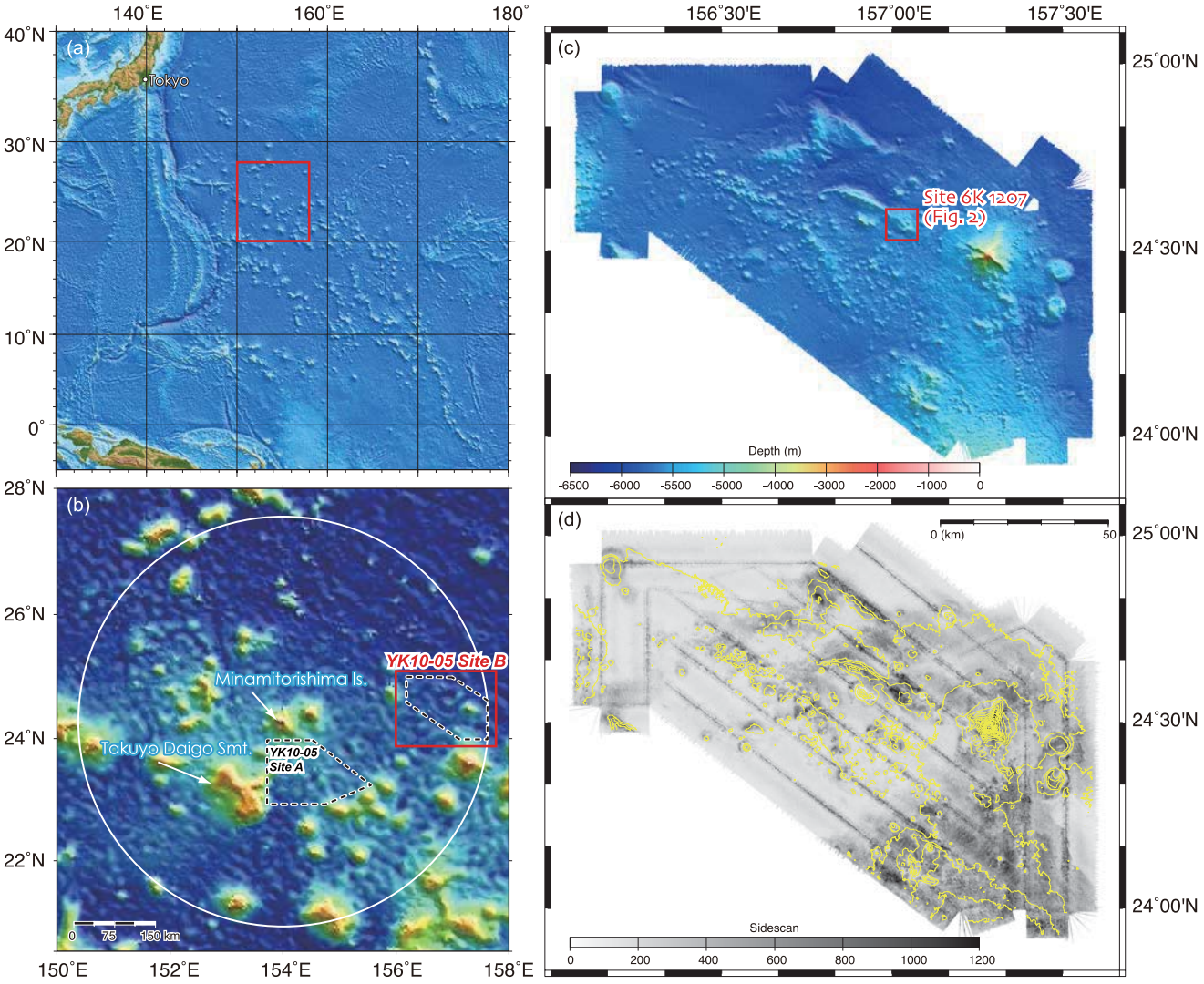

Fig. 1. Maps of the dense ferromanganese nodule field in the Japanese Exclusive Economic Zone around Minamitorishima Island. (a) Location map showing Japan (upper left) and red outline of area shown in (b). (b) Detail of (a) showing Minamitorishima Island, the Japanese EEZ (within the white circle), and sites surveyed during cruise YK10-05 of R/V Yokosuka. Bathymetric data are from ETOPO2 (NOAA National Geophysical Data Center; http://www.ngdc.noaa.gov/). (c) Bathymetric and (d) acoustic reflectivity maps of the area outlined in red in (b), on the basis of data collected by a multi narrow beam system SeaBeam2122.004 during cruise YK10-05.

Field Observations and Sampling

In precise bathymetric data recently acquired by the Japan Coast Guard, clusters of small conical knolls or seamounts were identified southeast of Minamitorishima Island by Oikawa and Morishita (2009), who remarked upon their morphological resemblance to petit-spot volcanoes in the northwestern Pacific (Hirano *et al.*, 2006, 2008). Cruise YK10-05 of *R/V Yokosuka* subsequently visited two sites in the area (sites A and B in Fig. 1) to perform acoustic surveys, using a multiple narrow-beam echo sounder system (SeaBeam2112.004) to map the bathymetry and acoustic reflectivity of the seafloor. During this cruise, we chose a small seamount approximately 300 km east of Minamitorishima Island at Site B (Site 6K 1207 in Fig. 1c) for investigation by *SHINKAI 6500*. The seamount at Site 6K 1207 is located on the Cretaceous Pacific Plate formed between 163 and 164 Ma (Müller *et al.*, 2008; Nakanishi *et al.*, 1989), that is in the region of the West Pacific Seamount Province (Koppers *et al.*, 2003) or the northernmost region of the Prime Crust Zone (Hein *et al.*, 2009, 2013).

The seamount at Site 6K 1207 rises about 400 m above the surrounding seafloor and has a ridge trending

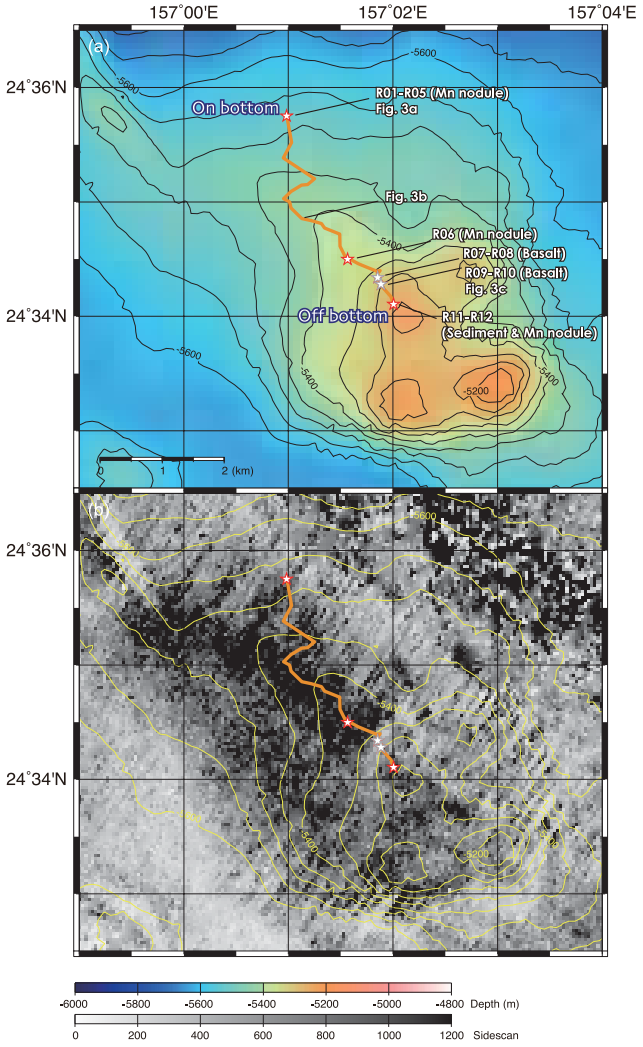

Fig. 2. Maps of (a) bathymetry and (b) acoustic reflectivity at Site 6K1207 derived from shipboard data. Orange line illustrates the survey track of SHINKAI 6500 dive No. 6K 1207. Locations of sampling sites are shown in red (for nodules) and gray (for crusts) open stars.

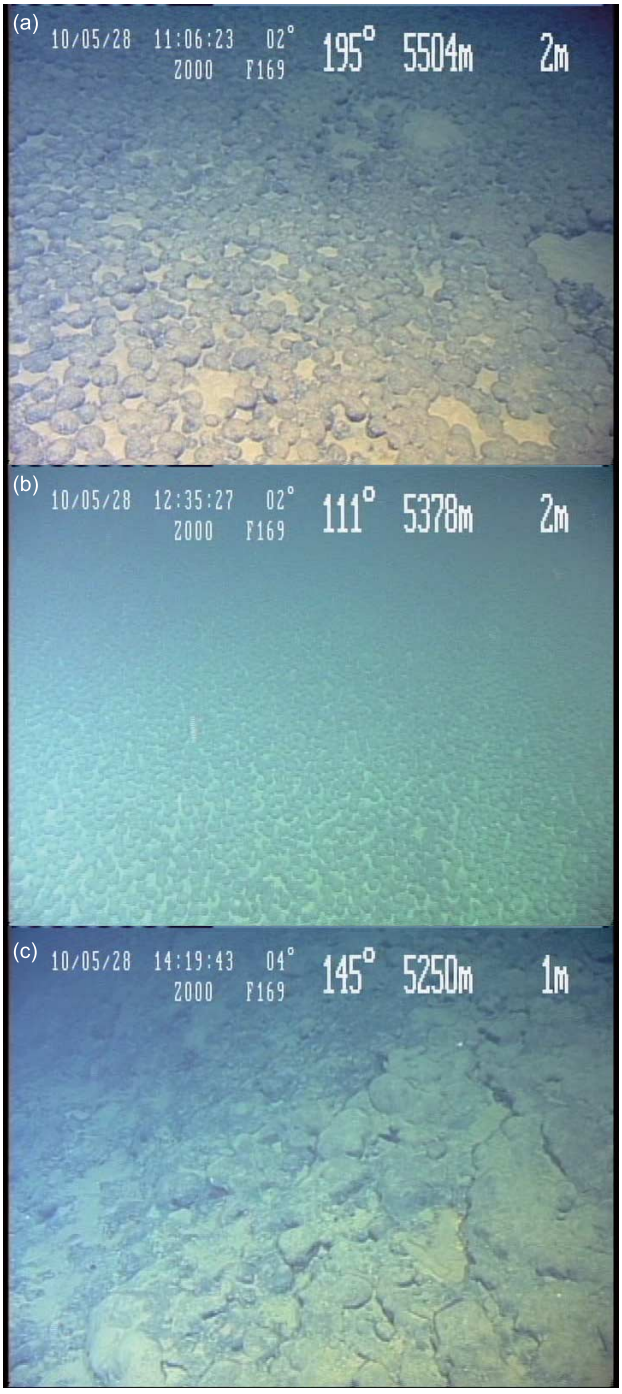

Fig. 3. Photographs showing representative seafloor at Site 6K 1207. Locations of each photo are shown in Fig. 2.

northwestward from its summit (Fig. 2a). Acoustic reflectivity was strong on the summit and slopes of this seamount (Fig. 2b). The *SHINKAI 6500* landed on the seafloor on the lower northern flank of the northwestern ridge in an area of strong acoustic reflections. There the seafloor was fully covered with hard, well rounded Fe-Mn nodules 5–10 cm in diameter along with very thin soft pelagic sediment (Fig. 3a). Some nodules were loosely connected by Fe-Mn crusts. Five nodule samples were collected using the manipulator at the landing point (R01, R02, R03, R04, and R05), and small fragments of nodules were collected using the scoop near the summit (R06) (Fig. 2, Tables 1 and 2). Nodules were densely distributed throughout the dive track (Fig. 3b). In contrast, scattered boulders were observed on the slightly steep slope near the summit (Fig. 3c). This slope had slightly lower acoustic reflectivity than the surrounding area. Four samples from boulders on this slope (R07, R08, R09, and R10) consisted of Fe-Mn crusts on a substrate of altered volcanic rocks (Fig. 2 and Table 2). Therefore, we inter-

Table 1. Locations of sampling points

Event	Latitude (N)	Longitude (E)	Depth (m)
Landing point (on bottom)	24°35.7433′	157°00.9824′	–5503
Collection of samples R01-05	24°35.7368′	157°00.9891′	–5503
Collection of sample R06	24°34.4847′	157°01.5693′	–5349
Collection of samples R07 and R08	24°34.3150′	157°01.8714′	–5306
Collection of samples R09 and R10	24°34.2604′	157°01.9038′	–5255
Collection of samples R11 and R12 (off bottom)	24°34.0950′	157°02.0163′	–5226

Table 2. Description of samples

Sample No.	Rock type	Diamiter (mm)			Wt (g)	Mn coating (mm)	Remarks
		X	Y	Z			
R01	Manganese nodule	80	110	90	850		With nucleus of silt
R02	Manganese nodule	100	90	70	800		With nucleus of silt
R03	Manganese nodule	100	70	70	750		With nucleus of silt
R04	Manganese nodule	70	70	90	700		With nucleus of silt
R05	Manganese nodule	80	75	90	750		Without nucleus?
R06	Manganese nodule				540		Collected using scoop
R07	Basalt	210	90	80	2150	13–32	With manganese crust
R08	Basalt	120	80	35	550	14	With manganese crust
R09	Basalt	200	140	160	5200	19	With manganese crust and soft silt
R10	Basalt	200	140	120	5500	12–50	With manganese crust and solid silt
R11	Sedimentary rock (silt)	90	50	35	200	7	With manganese crust
R12	Manganese nodule	90	60	40	400		With nucleus of silt

pret these boulders as pillow lavas, indicating that this small seamount was formed by volcanic activity. A sample of Fe-Mn crust on a substrate of sedimentary rocks (R11) and a nodule (R12) were collected on the summit (Fig. 2, and Tables 1 and 2).

The large nodules generally consist of three more or less concentric layers, designated L0 to L2 from the surface to the core (Fig. 4). The innermost layer L2 has a porous texture, with the pores containing brown sediment. It is covered by layer L1, consisting of massive black material. Blanketing this is the mottled and sediment-filled layer L0. The texture of each layers was observed under a microscope (Fig. 5). L2 is composed of dendritic grown δ-MnO_2 (showing dark grey color; e.g., Usui, 1983; Usui *et al*., 1987) and large pores and vugs containing biogenic and detrital (clay minerals) grains. δ-MnO_2 in L1 show parallel to subparallel growth laminations. The number and size of pores and vugs are drastically decreased in L1 compared to L2. In L0, δ-MnO_2 show petaline growth laminations. The openings between columns of δ-MnO_2 are stuffed by biogenic and detrital grains.

METHODS

We selected two representatives for large (R01 and R02, Fig. 4) and small nodules (R06, Supplementary Fig. S1). As mentioned in the previous section, other nodule samples, except for R06 and R12, were collected at the same sampling site for samples R01 and R02. R12 was eliminated for chemical analysis, because a large number of inclusions (possibly pelagic sediment) were observed. Samples R01 and R02 were cut vertically in half on board. To determine compositional changes from the center to the rim of the nodules, the interior was further split into ten slabs, each slightly less than 5 mm thick from subsample 01 at the top (seawater side) to subsample 10 at the bottom (sediment side) (Fig. 4). The two outermost subsamples (01 and 10) correspond closely to layer L0, the next two inner subsamples (02 and 09) match layer L1, and the remaining subsamples correspond to layer L2. The nucleus material in subsamples 05, 06, and 07 was carefully separated by hand-picking before analyzing the remainder. Whole of two pieces of R06 (R06a and R06b) were also analyzed without further separation, because a large nucleus was not observed. In addition, Fe-Mn crusts adhering to basalt samples R07, R08, R09, and R10 (Fig. S1) were analyzed for comparison with the nodules. A slab of ~5-mm-thickness containing the entire sequence of the Fe-Mn crust from the bottom to the surface was cut from each of these samples.

All of the cut samples were carefully polished with a

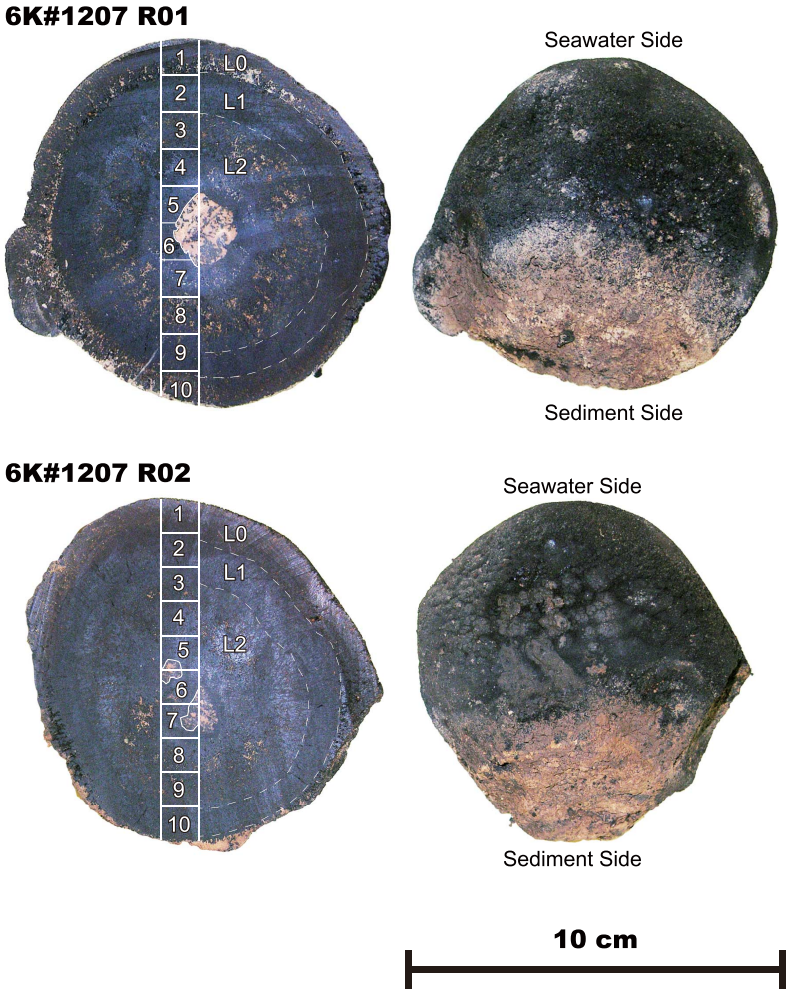

Fig. 4. Photographs of samples R01 (upper) and R02 (lower) showing vertical cross sections (left) and side views of counterpart (right). Numbered white squares show positions of sub-sampling for geochemical analysis. The nucleus portions, outlined in white within subsamples 05, 06, and 07, were separated from the samples before analysis. Dashed concentric circles illustrate boundaries of layers L0 to L2.

diamond plate to remove any contamination from the saw on the cut surface. After rinsing with ultra high purity water (18 MΩ-cm) and air-drying, the samples were pulverized in an agate mortar prior to major and trace element analyses.

Abundances of major and trace elements were determined using an Agilent 7500c inductively coupled plasma mass spectrometer (ICP-MS) at the Department of Systems Innovation, the University of Tokyo, following procedures described by Kato *et al*. (2005, 2011b). After drying the powdered samples at 110°C for ~12 h, 0.010 g subsamples were dissolved by HNO_3-HF-$HClO_4$ digestion in tightly sealed 12 mL Teflon PFA screw-cap beakers, and heated for several hours on a hot plate at 110°C. The dissolved sample was then progressively evaporated at 110°C for 12 h, 160°C for 6 h, and 190°C until dryness. Subsequently, 2 mL aqua regia was added to the residue, which was heated at 110°C for 12 h, then evaporated at 90°C until dry. The residue was then dissolved with 4 mL of HNO_3 and 1 mL of HCl, and the solution was diluted to 1:100,000 (for nodules) or 1:20,000 (for crust) by mass using ultra high purity water (18 MΩ-cm). Spectral overlaps from oxides and hydroxides ($^{44}Ca^{16}O$ on ^{60}Ni, $^{47}Ti^{16}O$ on ^{63}Cu, $^{50}Ti^{16}O$ on ^{66}Zn, $^{135}Ba^{16}O$ and $^{134}Ba^{16}O^{1}H$ on ^{151}Eu, $^{137}Ba^{16}O$ and $^{136}Ba^{16}O^{1}H$ on ^{153}Eu, $^{141}Pr^{16}O$ and $^{140}Ce^{16}O^{1}H$ on ^{157}Gd, $^{143}Nd^{16}O$ on ^{159}Tb, and $^{165}Ho^{16}O$ on ^{181}Ta) were corrected following Aries *et al*. (2000). Analyses of reference material JB-2, issued by the Geological Survey of Japan, were generally within 2% of accepted values, and reproducibility of replicate analyses (n = 5) was typically <3% of the relative standard deviation (RSD). Results of the analyses are listed in Table 3. Because our analysis demonstrated contamination from the nucleus of the nodule in subsample R02-

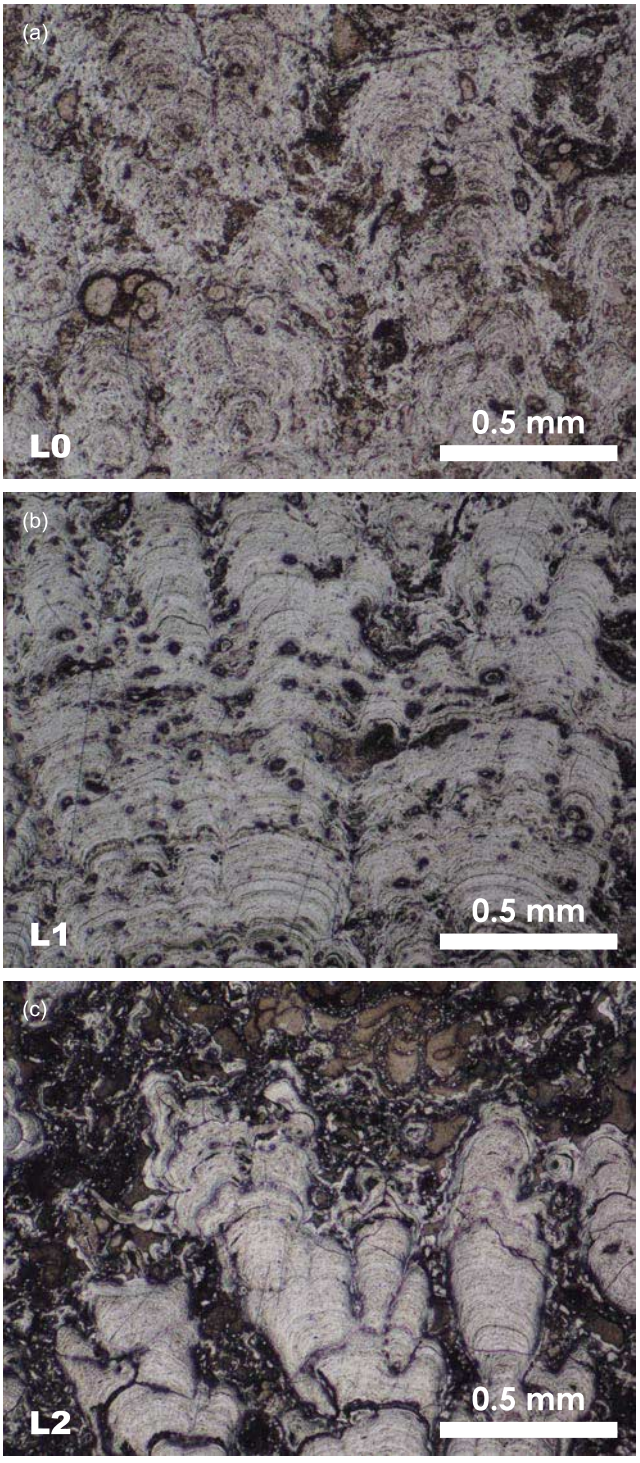

Fig. 5. Photomicrographs of the sample R02 showing features of texture of layers L0 (a), L1 (b), and L2 (c).

06, results from that subsample were discarded.

Bulk nodule compositions for samples R01 and R02 (Table 3) were calculated assuming a sphere separated into eight hemispherical shells corresponding in composition to subsamples 01, 02, 03, 04, 07, 08, 09, and 10, and a center corresponding to subsamples 05 and 06. The nominal diameter of this sphere was 9.5 cm for R01 and 8.5 cm for R02, values that were intermediate between the maximum and minimum dimensions of the nodules measured on board (Table 2). Mean density was 1.89 for R01 and 2.48 for R02 on the basis of their masses determined on board (Table 2) and their diameters. The composition of subsample R02-06 was assumed to be equal to that of subsample R02-05. In addition, the compositions of R06-a and R06-b were averaged to represent R06 (Table 3).

Results and Discussion

General geochemical features of nodules

We compare the general geochemical features of nodules from Site 6K 1207 and nodules and crusts from other localities in Fig. 6. The center of nodules from Site 6K 1207 (Fig. 6a, subsamples R01-6 and R02-5) have Mn/Fe ratios of 1.65–1.84 and are enriched in Ni compared to Co and Cu. In the observation of slightly high Mn/Fe and Ni contents in the center of nodules, they resemble nodules formed solely by diagenetic mechanisms (e.g., for nodules from the Peru Basin) or by mixed diagenesis and hydrogenetic (e.g., for nodules from CCZ) Fe-Mn precipitation (Fig. 6b). However, the Mn/Fe ratio and Cu abundance of the center of the nodules from Site 6K 1207 are lower than those of diagenetic nodules from other regions (e.g., Calvert and Price, 1977; Hein *et al*., 2013; Bau *et al*., 2014). Compared to the center, the rims of the nodules from Site 6K 1207 (Fig. 6a, subsamples R01-01, R01-10, R02-01, and R02-10) have lower Mn/Fe ratios (0.78–1.12) and Ni concentrations, and higher Co concentrations. These features, especially on the upper rims, are similar to those of hydrogenetic Fe-Mn crusts (Fig. 6c; Hein *et al*., 2013; Tokumaru *et al*., 2015; Nozaki *et al*., 2016).

The REE plus Y (REY) profiles of bulk nodules from Site 6K 1207, normalized to post-Archean average Australian shale (PAAS; Taylor and McLennan, 1985), display relative depletion in light REE (LREE) and positive Ce and negative Y anomalies (Fig. 6a), although the Y anomaly is smaller in subsamples 05 and 06 around the nucleus than in the other subsamples (Fig. 6b). Average concentrations of all the REY in nodules from Site 6K 1207 are higher than those in the Fe-Mn nodules from other regions such as the CCZ and Peru Basin (Bau *et al*., 2014) (Figs. 6b and 7), and similar to those of the non-phosphatized Fe-Mn crusts (Hein *et al*., 2013; Bau *et al*., 2014) (Figs. 6a and 6c). All of these observations suggest that Fe-Mn nodules at Site 6K 1207 did not follow a simple growth process. Consequently, their bulk composition is not typical of diagenetic Fe-Mn nodules (Fig.

6b) and is relatively similar to the composition of hydrogenetic Fe-Mn crust (Fig. 6c).

Compositional change through the growth of nodules

Detailed cross-sectional compositional profiles of nodules from Site 6K 1207 are shown for comparison with other nodules and crusts in Fig. 8. Elements including Ti, Co, As, REE other than Ce, Th, U, and Pb have the same pattern as Fe, concentrating in the nodule rim rather than the center. Among these, REEs and Pb are slightly enriched in the innermost part around the nucleus. In contrast, Al, P, Ca, Ni, Zn, Y, Mo, Ce, and W resemble Mn in having concentrations that are high in the center and decreasing toward the rim. The negative Y anomaly decreases from the surface (subsamples 01 and 10) to the nucleus (subsamples 05 and 06) (Figs. 7 and 8). Only Cu is the only exception to these tendencies, concentrating in the bottom rim of the nodule and decreasing from the center to the top rim (Fig. 8).

Geochemical trends within the nodules from Site 6K 1207 differ from those of the nodule rim, as well as nodules from other regions (Figs. 6 and 7). In comparison to nodules from CCZ, the most critical observation is that enrichment of Mn, Ni, Zn, Mo, and Cu in center of the Site 6K 1207 nodules is less pronounced whereas other elements including REY have higher concentrations. Halbach *et al*. (1981) reported that enrichment of Ni and Cu increases with Mn/Fe ratio up to about Mn/Fe = 5, and that a Mn/Fe ratio of 2.5 separates predominantly hydrogenetic nodules from the hybrid and the diagenetic nodules. Therefore, the lower Mn/Fe ratio (<2.5) and lesser enrichment in Mn, Ni, Zn, Mo, and Cu of Site 6K 1207 nodule centers suggest that diagenetic Fe-Mn-(oxyhydr)oxide precipitation did not persist through all stages of nodule growth.

That the Site 6K 1207 nodules have a growth history similar to that of Fe-Mn crusts is further suggested by their structural change from center to rim, and by comparison with hydrogenetic Fe-Mn crusts from the central and western equatorial Pacific. These Pacific seamounts crusts generally consist of a lower (older) phosphatized layer and an upper (younger) non-phosphatized layer (e.g., McMurtry *et al*., 1994; Koschinsky *et al*., 1997; Hein *et al*., 1993, 1999). Recent detailed descriptions (Pan *et al*., 2005; Kim *et al*., 2005, 2006), however, have shown that each of these layers is itself divided into two distinct layers for a total of four layers. The younger two layers of Fe-Mn crust, which formed after phosphatization by carbonate fluorapatite, are respectively characterized by mottled and porous or vuggy (inner; Layer 2), and massive (outer; Layer 1) texture (Pan *et al*., 2005; Kim *et al*., 2005, 2006). Similar porous sediment-filled (inner) and massive (outer) layers are also observed in Fe-Mn crust especially from deeper depths (2209–2987 m) of the

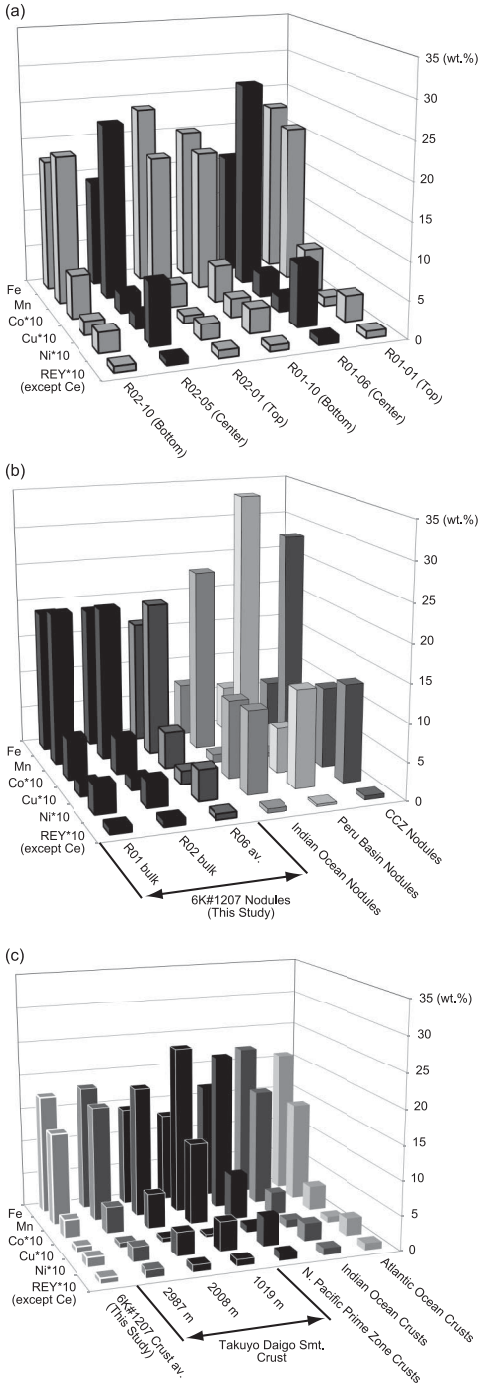

*Fig. 6. Block diagrams showing composition of Fe, Mn, Co, Cu, Ni, and REE (other than Ce) plus Y of (a) Fe-Mn nodules from Site 6K1207 and (b) nodules and (c) crusts from other locations. Fe-Mn nodule data from the Clarion and Clipperton Fracture Zone (CCZ), Peru Basin, and Indian Ocean, and crusts from the Atlantic, Indian, and northern Pacific (prime zone) oceans are from Hein et al. (2013). Hidden datum of Co*10 of the nodules from the CCZ and the Peru Basin in (b) is 2.098 and 0.475 (Hein et al., 2013), respectively. Surface data (3 mm thickness) of Fe-Mn crusts from Takuyo Daigo Seamount in the western Pacific are from Tokumaru et al. (2015) and Nozaki et al. (2016).*

Table 3. Bulk compositions for ferromanganese nodules and crust collected from Site 6K 01207

Sample No.	R01-01	R01-02	R01-03	R01-04	R01-05	R01-06	R01-07	R01-08	R01-09	R01-10	R01 bulk*	R02-01	R02-02	R02-03	R02-04
Lithology	Nodule	Nodule	Nodule	Nodule	Nodule	Nodule	Nodule	Nodule	Nodule	Nodule		Nodule	Nodule	Nodule	Nodule
Na (wt.%)	1.84	1.50	2.22	2.32	2.35	2.71	2.46	2.13	1.90	1.69	1.85	1.66	1.76	2.27	2.25
Mg	1.81	1.20	1.62	1.99	1.98	2.36	1.88	1.49	1.46	1.56	1.58	1.47	1.42	1.64	1.71
Al	3.50	2.34	3.86	4.82	4.90	5.96	4.94	3.54	2.84	3.33	3.31	2.58	2.71	3.58	4.50
P	0.39	0.30	0.47	0.51	0.55	0.61	0.42	0.31	0.39	0.35	0.37	0.43	0.41	0.47	0.42
K	1.13	0.64	0.94	1.20	1.17	1.38	1.30	0.90	0.76	0.93	0.93	0.82	0.74	0.98	1.12
Ca	2.72	2.11	2.71	3.11	3.00	3.51	3.30	2.84	2.65	2.33	2.56	2.43	2.37	3.02	2.90
Sc (ppm)	17.8	11.8	18.5	25.8	26.8	31.6	28.5	18.6	16.5	12.7	16.2	14.2	16.1	15.2	21.6
Ti (wt.%)	1.25	1.30	1.15	0.78	0.87	1.08	0.89	1.22	1.66	1.22	1.28	1.02	1.29	1.45	0.94
V (ppm)	625	459	477	452	430	534	517	558	637	577	565	664	629	584	469
Cr	25.2	5.34	8.95	63.1	39.9	18.0	18.7	14.8	b.d.l.	9.47		7.28	b.d.l.	3.62	16.7
Mn (wt.%)	21.0	17.8	21.1	22.6	23.4	27.4	24.2	21.0	22.3	18.6	20.3	18.5	20.0	23.5	20.9
Fe	22.7	15.9	14.3	12.0	12.7	16.0	14.2	14.7	20.2	20.2	18.9	23.8	21.2	17.6	13.3
Co (ppm)	5832	5390	5233	2471	2345	3170	3031	5708	6506	4925	5393	3088	4606	6342	3745
Ni	3476	2782	4883	7816	7345	8388	7495	4573	3041	3317	3729	2064	2907	4856	5847
Cu	1237	1167	1628	1958	1808	2054	1841	1548	1816	2523	1722	1013	1231	1920	1802
Zn	462	436	458	811	841	794	632	566	512	639	534	642	661	817	708
As	297	191	173	154	147	177	180	177	245	235	232	314	259	216	168
Rb	36.3	16.5	20.1	25.8	25.0	27.5	27.2	16.5	13.4	26.8	24.3	22.9	18.6	16.8	24.0
Sr	1162	1008	1026	943	1001	1204	1038	1045	1266	958	1076	1198	1193	1211	963
Y	163	137	158	191	182	216	209	155	160	134	153	168	177	169	183
Zr	634	523	535	513	478	740	599	564	526	486	548	562	551	434	464
Nb	62.6	62.4	75.0	55.7	55.8	72.5	65.7	78.1	72.3	73.6	68.7	60.7	69.3	77.6	67.6
Mo	339	342	473	586	511	598	531	505	456	329	391	369	428	519	469
Ag	0.03	0.12	b.d.l.	0.02	b.d.l.	0.07	0.11	b.d.l.	b.d.l.	b.d.l.		0.02	b.d.l.	0.06	0.02
Cs	3.07	1.31	1.42	1.84	1.69	1.90	2.11	1.20	1.37	2.56	3.98	2.01	1.78	1.26	1.49
Ba	1183	1189	1251	1309	1519	1899	1374	1415	1645	1342	1327	1262	1357	1481	1185
La	231	199	169	174	179	218	192	176	248	204	210	249	254	205	159
Ce	1939	1473	1396	1827	2321	2750	1960	1416	1831	1485	1665	1693	1628	1612	1518
Pr	59.1	46.5	42.0	44.9	45.8	55.7	48.6	43.4	58.8	50.7	51.9	64.4	62.1	48.2	40.9
Nd	228	181	163	180	183	218	192	164	225	194	200	256	240	190	161
Sm	52.8	40.4	36.7	41.6	41.8	51.2	45.1	37.3	51.0	44.3	45.7	60.2	54.0	41.5	37.2
Eu	12.8	9.66	8.97	10.1	9.94	11.9	11.0	9.2	12.5	11.0	11.2	14.6	13.0	9.87	8.99
Gd	54.1	42.7	39.0	43.7	43.0	52.2	46.7	39.0	51.8	45.7	47.2	60.7	56.8	44.5	40.8
Tb	8.62	6.74	5.94	6.52	6.39	7.50	7.09	6.06	8.34	7.46	7.50	9.68	9.00	6.86	6.09
Dy	50.0	40.3	36.8	39.5	37.1	44.0	43.2	37.4	51.0	43.7	44.7	56.0	54.1	42.3	36.3
Ho	9.61	8.03	7.36	7.70	7.21	8.75	8.64	7.33	9.95	8.43	8.70	10.24	10.43	8.44	7.25
Er	26.8	22.7	20.7	21.9	20.9	24.7	24.5	21.1	27.7	23.9	24.5	29.1	29.5	24.6	21.0
Tm	3.91	3.47	3.08	3.10	2.89	3.52	3.35	3.13	4.18	3.45	3.61	4.19	4.29	3.64	3.03
Yb	24.8	22.1	20.5	20.0	19.2	23.6	21.9	20.3	27.3	23.0	23.4	26.5	28.2	23.6	19.8
Lu	3.74	3.47	3.10	3.05	2.95	3.55	3.46	3.05	4.15	3.45	3.56	4.01	4.11	3.51	3.01
Hf	10.2	8.19	9.65	8.09	7.14	11.36	9.88	10.07	8.19	8.92	9.15	8.60	8.52	6.98	8.08
Ta	1.02	0.86	1.08	0.55	0.34	1.27	0.92	0.93	0.44	0.53	0.77	0.24	0.42	0.38	0.44
W	51.9	62.5	79.1	92.9	82.9	95.9	80.5	79.4	76.7	45.4	62.0	59.3	74.0	85.3	74.1
Tl	129	141	177	159	148	171	174	177	154	119	142	64.5	131	203	179
Pb	1291	930	694	709	959	1195	738	708	1131	1073	1038	1395	1171	908	644
Th	95.1	51.4	24.7	29.6	30.3	35.1	33.8	22.9	60.5	65.3	61.4	102.0	69.6	37.3	27.1
U	10.4	9.72	8.06	5.74	5.59	6.65	6.46	8.37	12.6	9.68	9.85	11.3	11.9	10.5	6.59
Mn/Fe	0.92	1.12	1.48	1.88	1.84	1.71	1.70	1.42	1.11	0.92	1.08	0.78	0.94	1.33	1.57
∑REY (except Ce)	928	763	715	787	780	939	856	722	940	798	835	1013	996	821	727

Sample No.	R02-05	R02-07	R02-08	R02-09	R02-10	R02 bulk*	R06-a	R06-b	R06 average	R07	R08	R09	R10	Crust average
Lithology	Nodule	Nodule	Nodule	Nodule	Nodule		Nodule	Nodule		Crust	Crust	Crust	Crust	
Na (wt.%)	2.42	2.57	2.02	2.35	1.68	1.90	2.18	1.97	2.07	1.33	1.18	1.19	1.21	1.23
Mg	1.97	2.12	1.51	1.66	1.33	1.50	1.64	1.51	1.58	1.08	0.96	1.02	0.87	0.98
Al	5.44	5.69	4.13	3.75	2.74	3.17	4.17	3.62	3.90	2.43	2.33	2.31	1.55	2.16
P	0.43	0.44	0.40	0.55	0.35	0.43	0.40	0.45	0.43	0.27	0.27	0.27	0.20	0.25
K	1.21	1.24	1.03	0.95	0.70	0.85	0.95	0.84	0.90	0.77	0.69	0.72	0.47	0.67
Ca	3.20	3.05	2.43	3.08	2.24	2.55	2.59	2.69	2.64	1.38	1.20	1.29	1.40	1.32
Sc (ppm)	25.3	27.5	20.1	15.8	12.3	15.5	17.3	12.4	14.9	14.1	14.2	13.5	12.3	13.5
Ti (wt.%)	0.99	1.02	0.76	1.38	1.37	1.21	1.14	1.39	1.26	1.02	0.84	0.90	1.16	0.98
V (ppm)	451	494	425	601	540	583	485	518	502	525	441	503	494	491
Cr	108	9.20	13.0	10.7	b.d.l.		4.97	5.90	5.44	13.1	14.2	18.0	7.0	13.1
Mn (wt.%)	23.5	24.2	18.3	23.8	19.8	20.4	20.4	20.7	20.5	14.2	11.9	12.5	15.3	13.5
Fe	14.2	14.6	11.7	16.0	17.6	18.7	15.3	17.4	16.3	19.3	16.3	18.5	15.7	17.5
Co (ppm)	2630	2652	2708	6757	5730	4721	4569	5082	4825	3127	2247	2343	3112	2707
Ni	8100	7375	5081	4855	2631	3485	4463	3797	4130	1440	1331	1252	1746	1442
Cu	1975	2084	1646	2080	1865	1588	1936	1636	1786	840	893	865	998	899
Zn	971	744	628	710	413	619	653	596	624	390	348	383	372	373
As	165	157	149	212	214	237	175	195	185	202	168	193	173	184
Rb	22.4	26.2	23.3	18.5	16.4	19.7	16.8	15.7	16.2	22.4	21.6	23.2	9.82	19.3
Sr	1049	1063	818	1153	1046	1114	1050	1156	1103	1001	841	920	1031	948
Y	189	178	147	152	142	160	142	160	151	202	175	188	123	172
Zr	624	635	485	468	406	492	479	532	506	604	531	592	517	561
Nb	70.2	68.9	58.8	82.5	59.7	66.6	71.5	73.4	72.5	61.6	52.2	59.1	58.5	57.9
Mo	481	498	413	585	418	444	426	399	412	263	204	228	328	255
Ag	b.d.l.	0.08	b.d.l.	0.07	b.d.l.		0.04	b.d.l.	0.04	b.d.l.	b.d.l.	b.d.l.	0.14	0.14
Cs	1.55	1.63	1.56	1.24	1.24	1.55	1.18	1.07	1.12	2.00	1.77	2.08	0.77	1.65
Ba	1583	1514	1015	1554	1377	1353	1340	1445	1392	1182	956	1086	1307	1133
La	180	174	127	174	204	210	169	212	191	203	173	189	133	174
Ce	2436	2429	1302	1573	1554	1618	1503	1622	1562	1482	1265	1406	1062	1304
Pr	46.6	44.2	33.8	41.8	48.9	52.0	40.3	50.4	45.4	56.0	49.1	53.8	42.0	50.2
Nd	180	177	130	159	191	203	154	192	173	217	189	207	169	195
Sm	43.2	39.7	30.8	37.1	41.3	46.3	33.5	42.0	37.7	51.5	45.6	50.3	40.2	46.9
Eu	10.3	9.90	7.63	8.83	10.2	11.2	8.5	10.7	9.61	12.7	11.3	12.4	10.1	11.6
Gd	43.0	41.2	32.7	38.3	45.3	48.5	36.9	45.0	41.0	53.2	47.9	52.3	45.3	49.7
Tb	6.33	6.33	4.94	5.98	7.10	7.60	5.84	7.10	6.47	8.36	7.30	8.15	6.77	7.65
Dy	37.5	36.4	30.0	35.9	43.5	45.4	35.2	43.5	39.4	49.4	43.6	47.9	40.6	45.4
Ho	7.54	7.04	5.82	7.12	8.51	8.72	7.16	8.61	7.89	9.47	8.21	8.88	7.76	8.58
Er	21.2	20.2	17.3	20.4	24.7	25.0	20.7	24.7	22.7	26.5	23.3	24.8	22.3	24.2
Tm	3.08	2.87	2.40	2.94	3.70	3.64	3.11	3.70	3.40	3.86	3.40	3.60	3.19	3.51
Yb	19.8	19.2	15.9	20.0	24.7	23.9	20.8	24.0	22.4	24.4	21.3	22.8	19.8	22.1
Lu	3.10	3.00	2.45	3.00	3.75	3.59	3.15	3.75	3.45	3.79	3.30	3.47	2.99	3.39
Hf	10.4	10.0	8.77	7.82	5.98	7.76	8.43	8.99	8.71	11.6	10.4	11.7	9.5	10.8
Ta	1.24	0.91	0.76	0.32	0.36	0.39	0.29	0.43	0.36	b.d.l.	b.d.l.	b.d.l.	b.d.l.	
W	77.3	76.0	60.5	87.6	62.2	69.5	76.4	73.9	75.2	49.7	36.7	41.1	62.2	47.4
Tl	163	160	130	178	136	131	183	170	177	50.7	44.3	47.6	97.8	60.1
Pb	970	950	520	808	1004	1039	763	945	854	1163	1010	1127	970	1068
Th	34.5	33.9	24.5	26.4	52.6	58.6	29.8	43.8	36.8	76.9	80.1	90.1	0.9	62.0
U	6.03	6.03	5.19	9.52	11.3	10.3	8.82	10.4	9.63	9.82	8.20	9.02	10.4	9.37
Mn/Fe	1.65	1.65	1.57	1.48	1.12	1.09	1.34	1.19	1.26	0.74	0.73	0.68	0.97	0.77
∑REY (except Ce)	791	758	589	706	798	849	680	828	754	921	802	872	665	815

b.d.l.: below detection limit.

**The bulk nodule compositions are calculated assuming a sphere separated into eight spherical shells.*

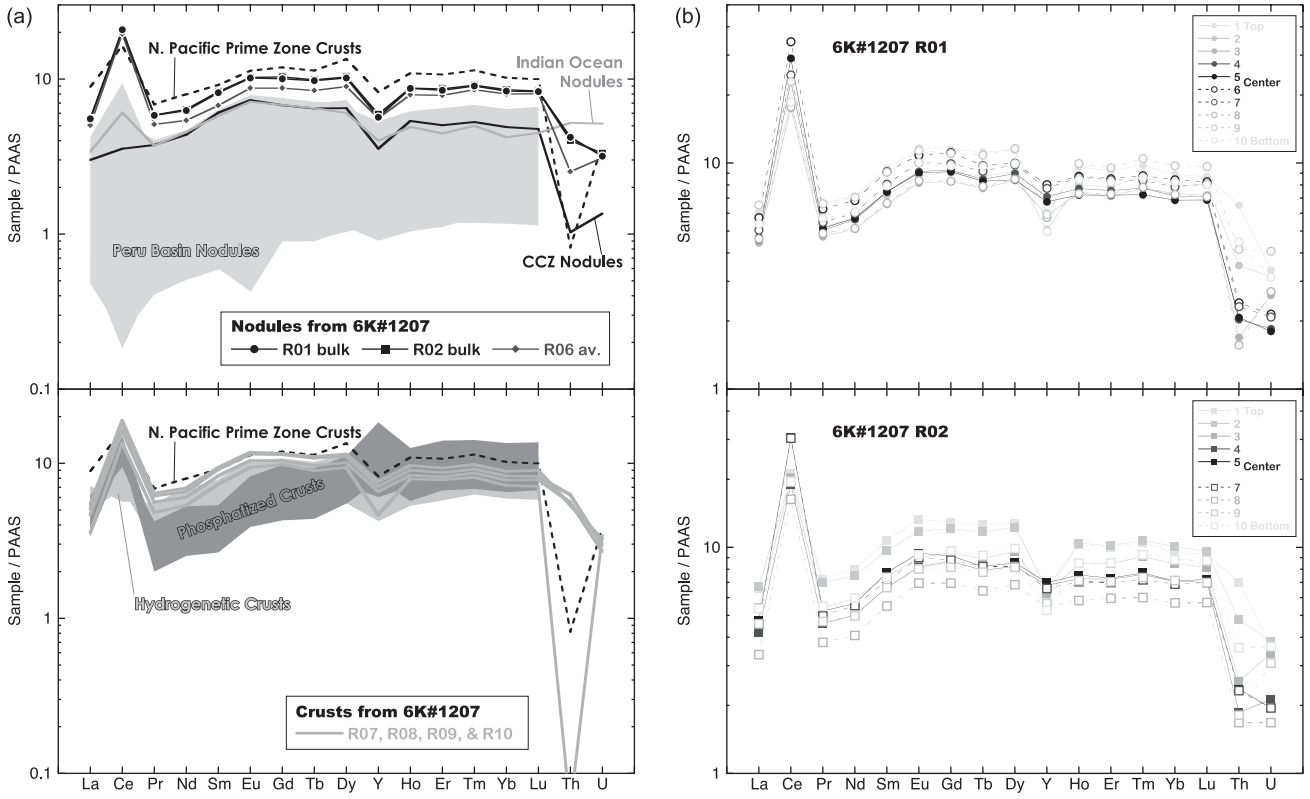

Fig. 7. REE, Y, Th, and U concentrations normalized to post-Archean average Australian shale (PAAS; Taylor and McLennan, 1985) for the ferromanganese (Fe-Mn) nodules from Site 6K 1207, and nodules and crusts from other locations. Fe-Mn nodule data from CCZ and Indian Ocean, and crusts from the northern Pacific prime zone are from Hein et al. (2013). Fe-Mn nodule data from the Peru Basin, and the hydrogenetic and phosphatized Fe-Mn crusts are from Bau et al. (1996, 2014).

Takuyo Daigo Seamount, which is located near the seamount at Site 6K 1207 (Tokumaru *et al*., 2015). In the case of the Takuyo Daigo Seamount, these two layers are further covered by an outermost mottled layer (Tokumaru *et al*., 2015). However, the three-layered-structure of Fe-Mn crust from the Takuyo Daigo Seamount completely corresponds to the three concentric layers (L0 to L2 from the surface to the center) of nodules from Site 1207 (Fig. 4). Based on microscopic observation (Fig. 5), the porous L2 and massive L1 features of our nodules is comparable to porous Layer 2 and massive Layer 1, respectively, of the Fe-Mn crust as described by Kim *et al*. (2005, 2006), although the texture of L0 of the nodules does not match to any layer of crust. We thus suggest that L1 and L2 of nodules from Site 6K 1207 and crust from the Takuyo Daigo Seamount correspond to Layers 1 and 2 of crusts from seamounts in the western equatorial Pacific.

The textural relationship between nodules from Site 6K 1207 and crust from the Takuyo Daigo Seamount (and seamounts in the western equatorial Pacific) is also supported by geochemical correspondences between them (Fig. 9). A simultaneous increase in Fe and decrease in Mn, Ni, and Cu from L2 to L0 of the seawater side of the Site 6K 1207 nodule (Figs. 8 and 9) is quite consistent with compositional change of those elements observed in the Takuyo crust (Nozaki *et al*., 2016) (Fig. 9). Furthermore, the most important geochemical feature on the Takuyo crusts during growth of L2 is that there are strong Ti concentration peaks (Fig. 9). Such a tendency is displayed by subsamples R01-05 and R01-03 of the Site 6K 1207 nodule (Figs. 8 and 9). This line of observations suggests that nodule and crust were formed by a common process. In the case of Fe-Mn crusts from the western equatorial Pacific, increasing Fe, decreasing Mn, Ni, and Cu, and strong Ti concentration peaks have been previously obtained (Pan *et al*., 2005; Kim *et al*., 2005, 2006). Kim *et al*. (2006) considered that the peak in Ti content, together with enrichment of Al, K, and Rb in Layer 2, indicated a high flux of detrital components when the crust-bearing site lay under the Intertropical Convergence Zone (ITCZ). In addition, Usui *et al*. (2007) showed that porous and mottled layers grew more rapidly than the massive layer on the basis of age determination using $^{10}Be/^{9}Be$ method. Enrichment of Al, K, and Rb is also observed in L2 of nodules from the Site 6K 1207 (Fig. 8; K and Rb not shown), in the same sense as in Layer 2 of

the western equatorial Pacific crust. Therefore, we consider that the porous and mottled texture, together with the geochemical features, of L2 of the nodules and Layer 2 of the crust to be formed by hydrogenetic precipitation with high flux of detrital components, probably when they were under the ITCZ. Thereafter, the massive texture of L1 nodules and Layer 1 of the crust is considered to be formed by hydrogenetic precipitation without detrital flux at out of the ITCZ.

The profiles in Figs. 8 and 9 show that the compositions of Co, Ni, W, and Mo in the rims of nodules from Site 6K 1207 (L0; subsample 01) resemble those on the surfaces of the Fe-Mn crust from the Takuyo Daigo Seamount (Tokumaru *et al*., 2015; Nozaki *et al*., 2016), especially crusts from deeper depths (e.g., 2967 m). Furthermore, Fe/Mn (Fig. 6) and the smooth surface of these nodules appear to indicate that the most recent phase of growth is solely by hydrogenetic precipitation of Fe-Mn-(oxyhydr)oxides (e.g., Halbach *et al*., 1981; Elderfield *et al*., 1981; Usui *et al*., 1987; Koschinsky and Halbach, 1995; Usui and Someya, 1997; Koschinsky and Hein, 2003; Kashiwabara *et al*., 2011, 2013). However, we consider the mottled texture of L0 of the nodules to be formed by rapid hydrogenetic precipitation (Usui *et al*., 2007), the same as L2. At the time of L0 formation, the nodule field at Site 6K 1207 were moved to higher latitudes and lower longitudes (closer to Asia) by plate motion rather than at the time of L2 and L1 formation. We thus consider that the high sedimentation rate during L0 formation was due to the production of terrigenous components such as eolian dust by westerly winds (e.g., Rea, 1994) and/or particulate materials by the riverine transport (e.g., Jeandel and Oelkers, 2015). In contrast, the absence of the outer-most mottled layer (corresponding to L0 of the nodules) on Fe-Mn crust from seamounts in the western equatorial Pacific (reported by Pan *et al*. (2005) and Kim *et al*. (2005, 2006)) could be explained by the absence of detrital flux from the Asian continent because of the lower latitude of these seamounts compared to Site 6K 1207.

We conclusively consider that our observations of geochemical signature essentially indicate a common hydrogenetic precipitation process for nodules from Site 6K 1207 and crust from Pacific seamounts. However, some differences are also recognized between them. Particularly, the abundance of Fe, Cu, Ti, Al, Ca, and Th of the Site 6K 1207 nodules are much greater than those of crust from the Takuyo Daigo Seamount (Fig. 9; Nozaki *et al*., 2016) or seamounts in the western Pacific (Pan *et al*., 2005; Kim *et al*., 2005, 2006), even though the tendencies of the compositional profiles of these elements are remarkably similar to one another. We think that the different abundances of these elements could be explained by differences in the sedimentary environment, which depended particularly on the water depth of the nodules (5503 m) and crust (e.g., 2967 m), as follows. The high level of abundance of Al, Ca, and K (K is not shown in Figs. 8 and 9) indicate constant contamination of clay minerals, as supported by microscopic observations (Fig. 5). Diagenetic enrichment explains the high Cu composition, especially on the bottom side (subsample 10) of the nodules. Both these phenomena occur because nodule formation occurs on pelagic sediments. Gradual enrichment in Fe, Ti, and Th with increasing water depth of crusts and nodules at the given, especially younger, layer (Fig. 9) should reflects the increasing of amount of dissolved Fe, Ti, and Th in seawater of the deep ocean (e.g., Nozaki *et al*., 1987; Orians *et al*., 1990; Johnson *et al*., 1997).

Constraints on formation age of nodules

Recent age determinations for the boundary between Layers 2 and 3 of Pacific Fe-Mn crusts (Hyeong *et al*., 2013) lead us to consider that the growth of the Layer 2 of crusts begins earlier on seamounts at higher latitudes rather than at lower latitudes. Such systematic latitudinal time migration on Layer 2 formation should be caused by earlier secession from the region of phosphatization by northwestward movement of the Pacific plate. As the seamount of Site 6K 1207 lies north of the seamounts studied by Hyeong *et al*. (2013), we can expect that the nodules at Site 6K 1207 began forming earlier than 32 Ma, the oldest age of the boundary between Layers 2 and 3 at the northernmost seamount (OSM 7) reported by Hyeong *et al*. (2013).

Hyeong *et al*. (2013) also showed that phosphatization on Pacific seamounts was intermittent between 36 and 12 Ma, putting the peak for phosphorite deposition near the Eocene/Oligocene transition (~34 Ma). Therefore, it is likely that layer L2 of the Site 6K 1207 nodules formed at a time when phosphatization of the Fe-Mn crusts continued at lower latitudes. Such a scenario would have resulted in slight enrichment of P and Ca around the nucleus of the nodules (subsamples R01-05 and R01-06) because of slightly high biogenic productivity in surface water that supplied biogenic phosphate to the abyssal environment (perhaps from the south). The slight enrichment in Y (as shown by a smaller negative Y anomaly) and Pb around the nucleus of the Site 6K 1207 nodules (Fig. 8) is also explained by an increased contribution of phosphate (Bau *et al*., 1996; Koschinsky *et al*., 1997; Koschinsky and Hein, 2003). Hein *et al*. (1999) reported that phosphatization of Fe-Mn crusts was not observed in samples collected from depths greater than 3000 m. If such observation indicates that phosphatization occurs only at shallow depth, the limited influence of phosphate on the center of Site 6K 1207 nodules can be interpreted as depth-dependence of phosphatization. Namely, there is a possibility that the formation of nodules had occurred

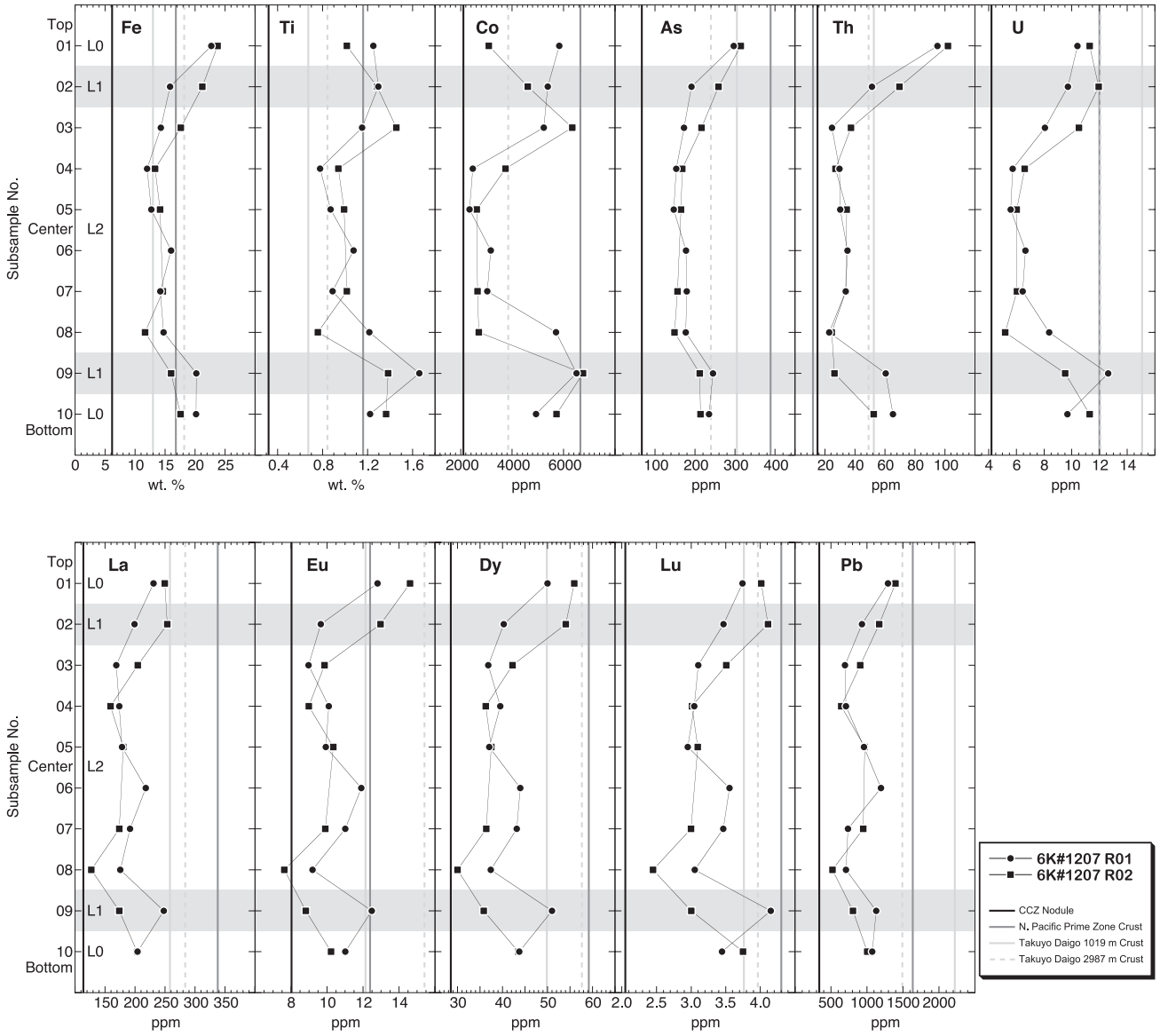

Fig. 8. Compositional profile of samples R01 and R02, with representative values from Fe-Mn nodules and crusts from the other locations (vertical lines). Fe-Mn nodule data from CCZ and Fe-Mn crusts from the northern Pacific prime zone are from Hein et al. (2013). Surface data (3 mm thickness) of the Fe-Mn crusts from Takuyo Daigo Seamount in the western Pacific are from Tokumaru et al. (2015). The first group of elements is affiliated with Fe, the second group is affiliated with Mn, Cu has an independent profile (see the text).

during the period of phosphatization of Fe-Mn crust at shallow depth. If we conduct future detailed investigations, especially on geochronology, the hydrogenitic Fe-Mn nodules in the EEZ around Minamitorishima Island are expected to contribute strongly to our understanding of the abyssal ocean environment and paleoclimate in the western Pacific.

Implications of nodules as critical metal resource

As previously discussed, the geochemical features of layer L2 of Site 6K1207 nodules are consistent with hydrogenetic precipitation of critical metals, with dilution by detrital (and possibly biogenic) components. However, the compositional profiles (Fig. 8) indicate that these dilution effects were less pronounced in the latter period of layer L2 formation, as shown by the increase of REY and Co with the decrease of Al, P, and Ca in subsample 03. Furthermore, it is clear that further enrichment in REY occurred during the rest of nodule formation. Therefore, we infer that dilution affected only the inner layers of the

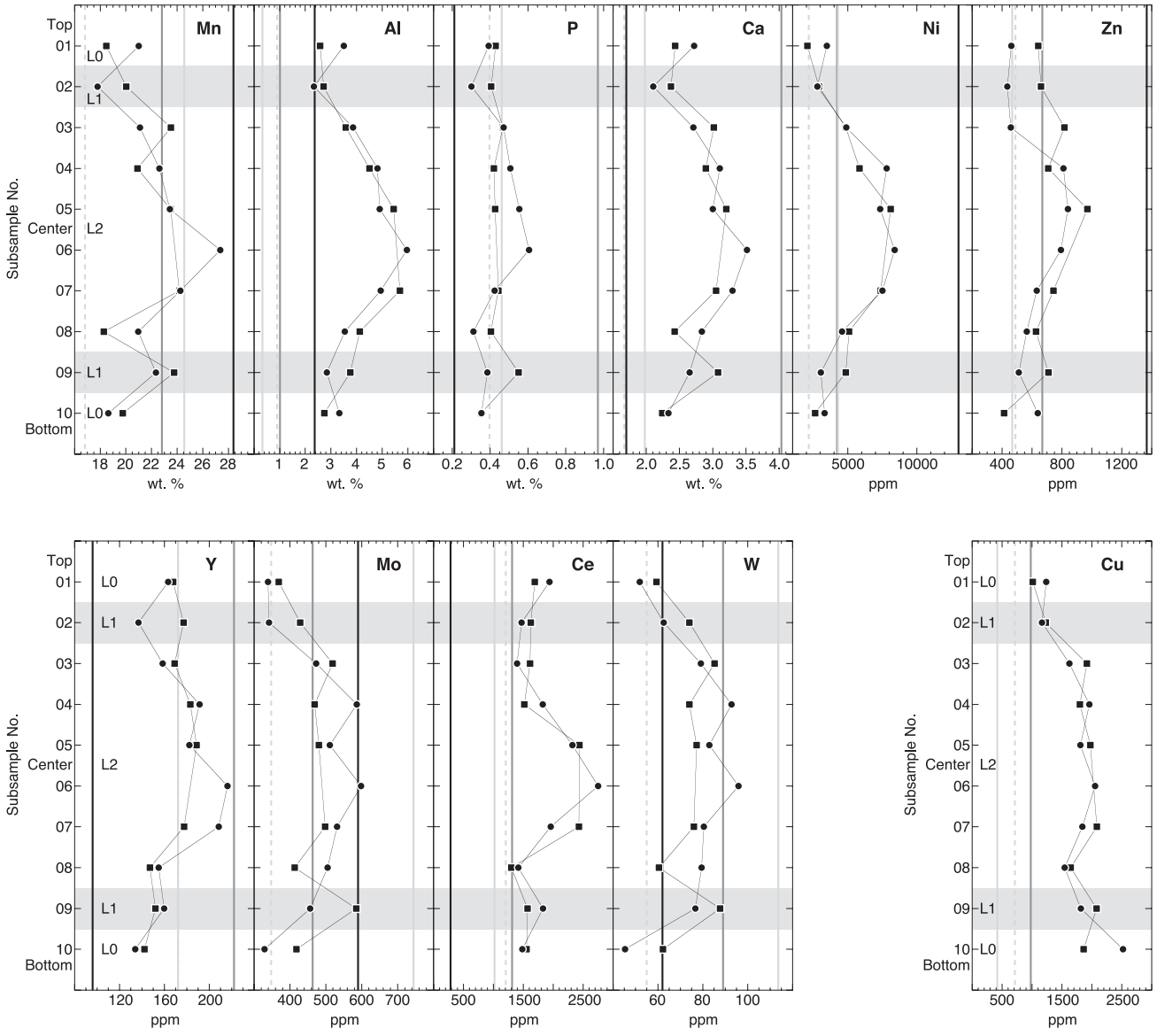

Fig. 8. (continued).

nodules, which are small in volume. Reduced dilution in these nodules at higher latitudes increases their potential as rare metal resources.

Our results show that the Fe-Mn nodules from Site 6K 1207 include moderate enrichments of critical metals, such as Co, Ni, Mo, and W, comparable to their levels in Fe-Mn crusts from the nearby Takuyo Daigo Seamount (Tokumaru *et al*., 2015; Nozaki *et al*., 2016). High concentrations of total REY (other than Ce) in bulk nodules match those of REY-rich mud collected from the central Pacific (Kato *et al*., 2011a) and the region south of Minamitorishima Island in the Japanese EEZ (Fujinaga *et al*., 2016). We propose that this dense nodule field is a newly identified area of high potential for mining of Fe-Mn nodules.

One notable fact learned during the geological survey of cruise YK10-05 is that the nodule field displays extremely strong acoustic reflectivity. This can be explained as a "mirror ball effect", whereby strong acoustic reflectivity regardless of seafloor slopes (topography) and acoustic beam angle represents specular returns from a concentration of hard, spherical nodules. This phenomenon should be considered in future exploration.

Recent acoustic surveys using a sub-bottom profiler in the Minamitorishima EEZ (Nakamura *et al*., 2016) showed that the seamount at Site 6K 1207 is situated within an area of T_I echo type. Nakamura *et al*. (2016) noted that the T_I-type sediment corresponds to the region

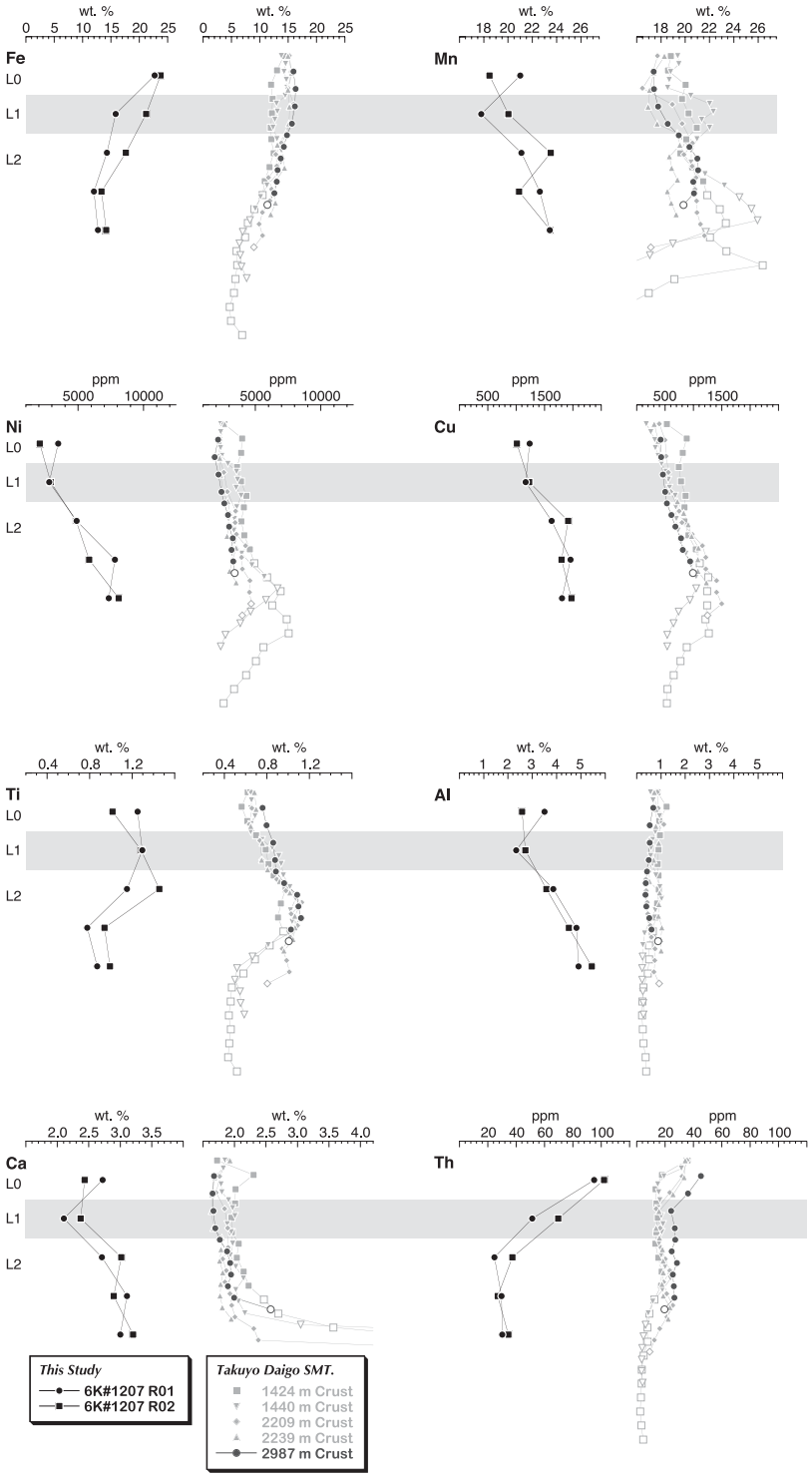

Fig. 9. Comparison of compositional profile between samples R01 and R02 (left) and the Fe-Mn crusts from Takuyo Daigo Seamount (SMT) in the western Pacific (right). Profiles for R01 and R02 are the same as the upper half (from subsample 01 to 05) of profiles in Fig. 8. Fe-Mn crust data from Takuyo Daigo Seamount are from Nozaki et al. (2016). Subsample data from the massive layer of the Fe-Mn crusts from Takuyo Daigo Seamount, except for the samples from 1424 and 1440 m water depths, are fixed to the position of L1 of the nodules, which are illustrated by gray bands. Subsample data at the upper boundary of porous and sediment-filled layers (corresponding to L2 of nodules) of the samples from 1424 and 1440 m water depths are fixed to the underside of the gray bands. Other data are proportionally posited, thus depth of profiles for Takuyo Daigo Seamount are not to scale in L0 and L2, even though they roughly correspond to those of the nodules. Open symbols for Fe-Mn crust data from Takuyo Daigo Seamount indicate subsamples with more than 1.1 wt.% P_2O_5.

where REY-rich mud is directly exposed on the seafloor, as reported by Iijima *et al*. (2016) and Fujinaga *et al*. (2016). From another point of view, geochemical studies of sediment cores drilled from the Indian Ocean (Yasukawa *et al*., 2015) showed that Fe-Mn-(oxyhydr)oxides contribute to form REY-rich mud as a critical component of REY-enrichment. In the case of the Indian Ocean REY-rich mud, co-enrichment of Fe, Mn, Co, and REY in bulk sediment correlates with increasing numbers of micro-ferromanganese nodules in sediment (Yasukawa *et al*., 2015). Similar accumulation of micro-ferromanganese nodules was also observed in the REY-rich mud cored from the Minamitorishima EEZ (Iijima *et al*., 2016). Therefore, coincidence of distribution of the Fe-Mn nodules and REY-rich mud, and the contribution of Fe-Mn-(oxyhydr)oxides to REY-rich mud formation imply a geologic and genetic relationship between them in the Minamitorishima EEZ. Further extensive exploration for Fe-Mn nodules using acoustic reflectivity, as a "simple" method, is expected to be a key to clarifying full potential of sea floor critical metal resources, including Fe-Mn crust and REY-rich mud in the Minamitorishima EEZ.

Conclusions

Our geological and geochemical investigations of the dense Fe-Mn nodule field approximately 300 km east of Minamitorishima Island have resulted in five major conclusions. (1) Seafloor with extremely strong acoustic reflectivity is densely covered with the Fe-Mn nodules, a feature that should be noted in future exploration. (2) Concentrations of Mn, Al, P, Ca, Ni, Zn, Y, Mo, Ce, and W are highest in the inner parts of nodules, whereas Fe, Ti, Co, As, REE other than Ce, Th, U, and Pb are enriched in the outer parts. (3) Textural and compositional changes over the growth history of the nodules are quite similar to those of the Fe-Mn crust on large seamounts in the western Pacific. Therefore, (4) the Fe-Mn nodules investigated in this study formed solely by hydrogenetic Fe-Mn-(oxyhydr)oxide precipitation that records paleoceanographic events probably beginning in the early Oligocene, and (5) these nodules have a high potential as a future metal resource, especially for Co, Ni, Mo, and W.

Acknowledgments—We gratefully acknowledge the shipboard scientific parties, captain, and crews of *R/V Yokosuka* and the operating team of *SHINKAI 6500* for their efficient work. S.M., K.F., and Y.K. are indebted to Y. Itabashi, D. Watanabe, and H. Liu for their invaluable assistance with ICP-MS analyses. We thank K. Yasukawa, J. Ohta, E. Uchida, and R. Watanabe for their helpful comments and discussions. This study was supported by the Japan Society for the Promotion of Science (JSPS) Grants-in-Aid for Scientific Research (S) No. 22226015 to Y.K. Instructive reviews and suggestions from two anonymous reviewers contributed greatly to this manuscript. We gratefully acknowledge T. Nozaki for handling of our manuscript and comments. GMT software (Wessel and Smith, 1998) was used to display bathymetric and acoustic reflection data.

References

Aries, S., Valladon, M., Polvé, M. and Dupré, B. (2000) A routine method for oxide and hydroxide interference corrections in ICP-MS chemical analysis of environmental and geological samples. *Geostandard. Newslett*. **24**, 19–31.

Bau, M., Koschinsky, A., Dulski, P. and Hein, J. R. (1996) Comparison of the partitioning behaviours of yttrium, rare earth elements, and titanium between hydrogenetic marine ferromanganese crusts and seawater. *Geochim. Cosmochim. Acta* **60**, 1709–1725.

Bau, M., Schmidt, K., Koschinsky, A., Hein, J., Kuhn, T. and Usui, A. (2014) Discriminating between different genetic types of marine ferro-manganese crusts and nodules based on rare earth elements and yttrium. *Chem. Geol*. **381**, 1–9.

Calvert, S. E. and Price, N. B. (1977) Geochemical variation in ferromanganese nodules and associated sediments from the Pacific Ocean. *Mar. Chem*. **5**, 43–74.

Elderfield, H., Hawkesworth, C. J., Greaves, M. J. and Calvert, S. E. (1981) Rare earth element geochemistry of oceanic ferromanganese nodules and associated sediments. *Geochim. Cosmochim. Acta* **45**, 513–528.

Fujinaga, K., Yasukawa, K., Nakamura, K., Machida, S., Takaya, Y., Ohta, J., Araki, S., Liu, H., Usami, R., Maki, R., Haraguchi, S., Nishio, Y., Usui, Y., Nozaki, T., Yamazaki, T., Ichiyama, Y., Ijiri, A., Inagaki, F., Machiyama, H., Iijima, K., Suzuki, K., Kato, Y. and KR13-02, MR13-E02 Leg 2 and KR14-02 Cruise Members (2016) Geochemistry of REY-rich mud in the Japanese Exclusive Economic Zone around Minamitorishima Island. *Geochem. J*. **50**, this issue, 575–590.

Halbach, P., Scherhag, C., Hebisch, U. and Marchig, V. (1981) Geochemical and mineralogical control of different genetic types of deep-sea nodules from the Pacific Ocean. *Mineral Deposita* **16**, 59–84.

Hein, J. R., Yeh, H.-W., Gunn, S. H., Sliter, W. V., Benninger, L. M. and Wang, C.-H. (1993) Two major Cenozoic episodes of phosphogenesis recorded in equatorial Pacific seamount deposits. *Paleoceanography* **8**, 293–311.

Hein, J. R., Koschinsky, A., Bau, M., Manheim, F. T., Kang, J. K. and Roberts, L. (1999) Cobalt-rich ferromanganese crusts in the Pacific. *Handbook of Marine Mineral Deposits* (Cronan, D. S., ed.), 239–279, CRC Press, Boca Raton, Florida.

Hein, J. R., Conrad, T. A. and Dunham, R. E. (2009) Seamount characteristics and mine-site model applied to exploration and mining-lease-block selection for cobalt-rich ferromanganese crusts. *Mar. Georesour. Geotechnol*. **27**, 160–176, doi:10.1080/10641190902852485.

Hein, J. R., Conrad, T. A. and Staudigel, H. (2010) Seamount mineral deposits, a source of rare metals for high-technology industries. *Oceanography* **23**, 184–189.

Hein, J. R., Mizell, K., Koschinsky, A. and Conrad, T. A. (2013)

Deep-ocean mineral deposits as a source of critical metals for high- and green-technology applications: Comparison with land-based resources. *Ore Geol. Rev*. **51**, 1–14.

Hirano, N., Takahashi, E., Yamamoto, J., Abe, N., Ingle, S. P., Kaneoka, I., Kimura, J.-I. Hirata, T., Ishii, T., Ogawa, Y., Machida, S. and Suyehiro, K. (2006) Volcanism in response to plate flexure. *Science* **313**, 1426–1428.

Hirano, N., Koppers, A. A. P., Takahashi, A., Fujiwara, T. and Nakanishi, M. (2008) Seamounts, knolls and petit spot monogenetic volcanoes on the subducting Pacific Plate. *Basin Res*. **20**, 543–553.

Hyeong, K., Kim, J., Yoo, C. M., Moon, J.-W. and Seo, I. (2013) Cenozoic history of phosphogenesis recorded in the ferromanganese crusts of central and western Pacific seamounts: Implications for deepwater circulation and phosphorus budgets. *Palaeogeogr. Palaeoclimatol. Palaeoecol*. **392**, 293–301.

Iijima, K., Yasukawa, K., Fujinaga, K., Nakamura, K., Machida, S., Takaya, Y., Ohta, J., Haraguchi, S., Nishio, Y., Usui, Y., Nozaki, T., Yamazaki, T., Ichiyama, Y., Ijiri, A., Inagaki, F., Machiyama, H., Suzuki, K., Kato, Y. and KR13-02 Cruise Members (2016) Discovery of extremely REY-rich mud in the western North Pacific Ocean. *Geochem. J*. **50**, this issue, 557–573.

Jeandel, C. and Oelkers, E. H. (2015) The influence of terrigenous particulate material dissolution on ocean chemistry and global element cycles. *Chem. Geol*. **395**, 50–66, doi:10.1016/j.chemgeo.2014.12.001.

Johnson, K. S., Gordon, R. M. and Coale, K. H. (1997) What controls dissolved iron concentrations in the world ocean? *Mar. Chem*. **57**, 137–161.

Kashiwabara, T., Takahashi, Y., Tanimizu, M. and Usui, A. (2011) Molecular-scale mechanisms of distribution and isotopic fractionation of molybdenum between seawater and ferromanganese oxides. *Geochim. Cosmochim. Acta* **75**, 5762–5784.

Kashiwabara, T., Takahashi, Y., Marcus, M. A., Uruga, T., Tanida, T., Terada, T. and Usui, A. (2013) Tungsten species in natural ferromanganese oxides related to its different behavior from molybdenum in oxic ocean. *Geochim. Cosmochim. Acta* **106**, 364–378.

Kato, Y., Fujinaga, K. and Suzuki, K. (2005) Major and trace element geochemistry and Os isotopic composition of metalliferous umbers from the Late Cretaceous Japanese accretionary complex. *Geochem. Geophys. Geosyst*. **6**, Q07004, doi:10.1029/2005GC000920.

Kato, Y., Fujinaga, K., Nakamura, K., Takaya, Y., Kitamura, K., Ohta, J., Toda, R., Nakashima, T. and Iwamori, H. (2011a) Deep-sea mud in the Pacific Ocean as a potential resource for rare-earth elements. *Nat. Geosci*. **4**, 535–539.

Kato, Y., Fujinaga, K. and Suzuki, K. (2011b) Marine Os isotopic fluctuations in the early Eocene greenhouse interval as recorded by metalliferous umbers from a Tertiary ophiolite in Japan. *Gondwana Res*. **20**, 594–607.

Kim, J., Hyeong, K., Yoo, C. M., Moon, J. W., Kim, K. H., Ko, Y. T. and Lee, I. (2005) Textural and geochemical characteristics of Fe-Mn crusts from four seamounts near the Marshall Islands, western Pacific. *Geosci. J*. **9**, 331–338.

Kim, J., Hyeong, K., Jung, H.-S., Moon, J.-W., Kim, K.-H. and Lee, I. (2006) Southward shift of the Intertropical Convergence Zone in the western Pacific during the late Tertiary: Evidence from ferromanganese crusts on seamounts west of the Marshall Islands. *Paleoceanography* **21**, PA4218.

Koppers, A. A. P., Staudigel, H., Pringle, M. S. and Wijbrans, J. R. (2003) Short-lived and discontinuous intraplate volcanism in the South Pacific: Hot spots or extensional volcanism? *Geochem. Geophys. Geosyst*. **4**, 1089, doi:10.1029/2003GC000533.

Koschinsky, A. and Halbach, P. (1995) Sequential leaching of marine ferromanganese precipitates: genetic implications. *Geochim. Cosmochim. Acta* **59**, 5113–5132.

Koschinsky, A. and Hein, J. R. (2003) Acquisition of elements from seawater by ferromanganese crusts: solid phase associations and seawater speciation. *Mar. Geol*. **198**, 331–351.

Koschinsky, A., Stascheit, A., Bau, M. and Halbach, P. (1997) Effects of phosphatization on the geochemical and mineralogical composition of marine ferromanganese crusts. *Geochim. Cosmochim. Acta* **61**, 4079–4094.

McMurtry, G. M., VonderHaar, D. L., Eisenhauer, A., Mahoney, J. J. and Yeh, H.-W. (1994) Cenozoic accumulation history of a Pacific ferromanganese crust. *Earth Planet. Sci. Lett*. **125**, 105–118.

Müller, R. D., Sdrolias, M., Gaina, C. and Roest, W. R. (2008) Age, spreading rates, and spreading asymmetry of the world's ocean crust. *Geochem. Geophys. Geosyst*. **9**, Q04006, doi:10.1029/2007GC001743.

Nakamura, K., Machida, S., Okino, K., Masaki, Y., Iijima, K., Suzuki, K. and Kato, Y. (2016) Acoustic characterization of pelagic sediments using sub-bottom profiler data: Implications for the distribution of REY-rich mud in the Minamitorishima EEZ, western Pacific. *Geochem. J*. **50**, this issue, 605–619.

Nakanishi, M., Tamaki, K. and Kobayashi, K. (1989) Mesozoic magnetic snomaly lineations and seafloor spreading history of the Northwestern Pacific. *J. Geophys. Res*. **94**, 15437–15462.

Nozaki, T., Tokumaru, A., Takaya, Y., Kato, Y., Suzuki, K. and Urabe, T. (2016) Major and trace element compositions and resource potential of ferromanganese crust at Takuyo Daigo Seamount, northwestern Pacific Ocean. *Geochem. J*., **50**, this issue, 527–537.

Nozaki, Y., Yang, H.-S. and Yamada, M. (1987) Scavenging of thorium in the ocean. *J. Geophys. Res*. **92**, 772–778.

Oikawa, M. and Morishita, T. (2009) Submarine topography in the east sea to the Minami-Tori Shima Island, Northwest Pacific Ocean. *Rep. Hydrogr. Oceanogr. Res*. **45**, 13–22 (in Japanese with English abstract).

Orians, K. J., Boyle, E. A. and Bruland, K. W. (1990) Dissolved titanium in the open ocean. *Nature* **348**, 322–325.

Pan, J., De Carlo, E. H., Yang, Y., Liu, S. and You, G. (2005) Effect of phosphatization on element concentration of cobalt-rich ferromanganese crusts. *Acta Geol. Sin*. **79**, 349–355.

Rea, D. K. (1994) The paleoclimatic record provided by eolian deposition in the deep sea: The geologic history of wind. *Rev. Geophys*. **32**, 159–195, doi:10.1029/93RG03257.

Taylor, S. R. and McLennan, S. M. (1985) *The Continental Crust: Its Composition and Evolution*. Blackwell Scientific

Publications, Oxford, 312 pp.
Tokumaru, A., Nozaki, T., Suzuki, K., Goto, K. T., Chang, Q., Kimura, J.-I., Takaya, Y., Kato, Y., Usui, A. and Urabe, T. (2015) Re-Os isotope geochemistry in the surface layers of ferromanganese crusts from the Takuyo Daigo Seamount, northwestern Pacific Ocean. *Geochem. J*. **49**, 233–241.
Usui, A. (1983) Regional variation of manganese nodules facies on the Wake-Tahiti transect: Morphological, chemical and mineralogical study. *Mar. Geol*. **54**, 27–51.
Usui, A. and Someya, M. (1997) Distribution and composition of marine hydrogenetic and hydrothermal manganese deposits in the northwest Pacific. *Manganese Mineralization: Geochemistry and Mineralogy of Terrestrial and Marine Deposits* (Nicholson, K., Hein, J. R., Bühn, B. and Dasgupta, S., eds.), *Geol. Soc. London Spec. Publ*. **119**, 177–198.
Usui, A., Nishimura, A., Tanahashi, M. and Terashima, S. (1987) Local variability of manganese nodule facies on small abyssal hills of the Central Pacific basin. *Mar. Geol*. **74**, 237–275.
Usui, A., Graham, I. J., Ditchburn, R. G., Zondervan, A., Shibasaki, H. and Hishida, H. (2007) Growth history and formation environments of ferromanganese deposits on the Philippine Sea Plate, northwest Pacific Ocean. *Island Arc* **16**, 420–430.
Wessel, P. and Smith, W. H. F. (1998) New, improved version of the generic mapping tools released. *Eos Trans. AGU* **79**, 579.
Yasukawa, K., Nakamura, K., Fujinaga, K., Machida, S., Ohta, J., Takaya, Y. and Kato, Y. (2015) Rare-earth, major, and trace element geochemistry of deep-sea sediments in the Indian Ocean: Implications for the potential distribution of REY-rich mud in the Indian Ocean. *Geochem. J*. **49**, 621–635.

Supplementary Materials

URL (http://www.terrapub.co.jp/journals/GJ/archives/data/50/MS419.pdf)
Figure S1